Self-Localization Method Using a Single Acoustic Ranging Sensor Based on Impulse Response and Doppler Effect

Atsushi Tsuchiya , *Graduate Student Member, IEEE*, Naoto Wakatsuki ,
Tadashi Ebihara , *Senior Member, IEEE*, Keiichi Zempo , *Member, IEEE*, and Koichi Mizutani

Abstract—This study aims to realize self-position estimation for indoor robots using only a single acoustic channel. When a single omnidirectional transmitter/receiver is used as an object detection sensor, detected objects are identified on concentric circles with the transmitter/receiver as the center point. Self-position estimation method using this sensor cannot use the directional information of the detected object. This fact makes it impossible to specify the robot's turning angle using environmental information. In this article, we propose a self-position estimation method using a single omnidirectional transmitter/receiver that can consider the direction of the reflected object by estimating the direction of the reflected wave from the Doppler effect generated during the robot's movement. The self-position estimation was implemented by using echo images of the direction of arrival of sound waves estimated from the Doppler effect and the distance of arrival of sound waves estimated from the impulse response and matching them with a previously generated map image. The accuracy of the proposed method was evaluated by simulation and experiment. In the simulation, an average position estimation error of 0.042 m was achieved; in the experiment, it was 0.051 m. Furthermore, experimental and simulation results show that using the Doppler effect contributes to self-position estimation accuracy.

Index Terms—Acoustic ranging sensor, Doppler effect, impulse response, indoor positioning, particle filter.

I. INTRODUCTION

MOBILE robots have already been introduced into indoor environments, such as construction sites and factories. Such robots need to measure their position to plan their path. Two methods have been proposed to measure self-position: one involves beacons [1], [2], [3], [4], [5], and the other, ranging sensors. Both methods have been studied, but the ranging sensor plays a vital role for mobile robots because it does not require the installation of a base station and can be used to detect actual obstacles.

Light detection and ranging (LiDAR), millimeter-wave radio detection and ranging (millimeter-wave radar), and ultrasonic sensors have been proposed as typical object detection sensors. LiDAR measures the distance to an object by measuring the

arrival time of a laser beam [6], [7], [8], [9], [10]. Time to digital converter (TDC) is used to measure the arrival time, and the resolution of TDC is several tens of picoseconds, which is on the order of centimeters in terms of distance. Angular scanning is achieved by changing the direction of the laser beam using mirrors. This mechanism enables LiDAR to achieve high angular resolution and a wide angular range. However, false detection is likely to occur in the presence of optical scatterers, such as fog or dust. They cannot be detected when optically transparent objects, such as glass, are used in indoor structures. Furthermore, since TDC measures the time difference of short pulses, it is not easy to distinguish them from pulses irradiated by other LiDARs.

Millimeter-wave radar is a ranging method that uses high-frequency, broadband radio waves to achieve high-distance resolution [11]. When millimeter-wave radar uses a 4-GHz bandwidth at a frequency of 79 GHz, the distance resolution is on the order of centimeters. On the other hand, the range-finding method using radio waves is subject to restrictions on frequency band and radio wave strength according to national laws. In addition, millimeter-wave radars require high-frequency circuits and high-performance analog-to-digital converter with high sampling frequencies to be built into the equipment.

Ultrasonic sensors use sound waves to measure distances [10], [12], [13]. The slow propagation time of sound waves makes it easy to achieve high-distance resolution. For example, a bandwidth of 10 kHz is sufficient to achieve the same level of distance resolution as LiDAR or millimeter-wave radar. This bandwidth can be achieved with an inexpensive audio interface. In recent years, high-resolution audio has become popular, and it is possible to achieve even higher accuracy in distance measurement with consumer devices. The phase modulation technique can be

used to prevent interference between other devices. In addition, many objects have very different acoustic impedances from air, so reflected waves can be obtained from many structures in the real world. On the other hand, sound waves take a long time to arrive, which increases the measurement time when measuring multiple points by angular scanning. Furthermore, it is difficult to achieve high angular resolution with sound waves because it is difficult to achieve sharp directivity like a laser. Thus, each sensor has its weak points. Therefore, in recent years, these sensors have often been combined to realize navigation for automatic robots, and it is essential to achieve high-ranging and position estimation accuracy with each elemental technology. In addition, the method of using sound waves is effective as a low-cost method to achieve highly accurate distance resolution, and it is an elemental technology that enhances the usability of navigation technology.

Self-position estimation methods and obstacle avoidance using ultrasonic sensors have long been studied in mobile robotics [12], [13], [14], [15], [16], [17], [18]. The arrival time of reflected waves obtained from ultrasonic sensors is registered in a cell on a map as a probability distribution of objects, and the self-position is estimated by matching the distribution [13], [16], [17]. However, it is generally difficult to achieve sufficient accuracy with a single ultrasonic sensor because it is difficult to sharpen the directivity of ultrasonic sensors and perform high-speed angular scanning. Since LiDAR has excellent directivity and is capable of high-speed angular scanning, it has been introduced as an alternative to ultrasonic sensors. Microphone arrays and parametric speakers have been proposed to solve directivity problems in ultrasonic sensors. The microphone array estimates the direction of arrival (DoA) of sound waves by processing the signals using a large number of microphones arranged in a cylindrical or linear shape [16], [18], [19], [20], [21], [22], [23], [24]. The parametric speaker achieves high directivity and long-distance propagation by self-demodulating ultrasonic waves from many ultrasonic transducers [25], [26]. These methods require a large number of time-synchronized audio interfaces. Furthermore, these methods require the placement of many microphones and loudspeakers, which significantly impairs the usability of ultrasonic sensors, which can be realized with simple configuration and low cost.

In recent years, methods have been proposed that use the impulse response of indoor spaces for all directions and not the arrival time of sound waves for a particular direction [27], [28], [29], [30], [31]. These methods can realize self-position estimation with a simple configuration of only a single loudspeaker and a microphone. However, they cannot correct the horizontal attitude angle of self-position because they are unable to identify the direction of reflected objects. In addition, the indoor environment generates numerous multipaths, which interfere with reflected waves. Therefore, different reflected waves arriving at the same time cannot be detected individually [32].

We therefore proposed a method for estimating object direction based on the Doppler effect using only a single loudspeaker and microphone [33], [34]. When a ranging sensor moves, the sound waves transmitted and received by that sensor generate the Doppler effect, determined by the sending and receiving
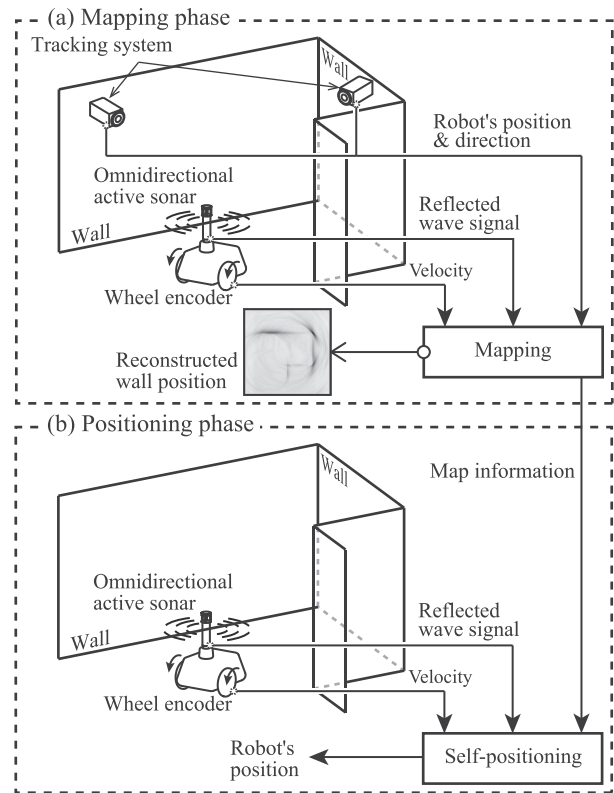

Fig. 1. Schematic diagram of mapping and positioning methods.

angles of the sound waves relative to the direction of movement. By measuring the magnitude of this Doppler effect, the DoA of each reflected wave can be determined. In addition, since this method can measure multiple reflected waves separately for each direction, it has robust performance against interference between reflected waves.

In this article, we propose a self-position estimation method using the DoA of reflected waves measured based on the Doppler effect and the time of arrival (ToA) measured based on the impulse response. The method consists of two phases: a mapping phase and a self-positioning phase. The mapping and self-positioning phases are shown in Fig. 1. The mobile robot has a wheel encoder to measure the linear and horizontal angular velocity, and a single loudspeaker and microphone to measure the reflected wave signals. The mapping phase uses a motion-tracking system to measure the absolute position of the mobile robot. Using the time-synchronized linear velocity, horizontal angular velocity, reflected wave signals, and absolute position, it generates a map for self-position estimation [34]. In the self-positioning phase, the motion tracking system is removed, and the self-position is estimated using only the sensors mounted on the mobile robot. In this phase, the map created in the mapping phase is used for self-position estimation.

Many acoustic ranging methods acquire DoA information with high angular resolution by applying control or signal processing to many acoustic channels to achieve self-position estimation. In contrast, our method uses the Doppler effect to obtain DoA information using only a single acoustic channel.
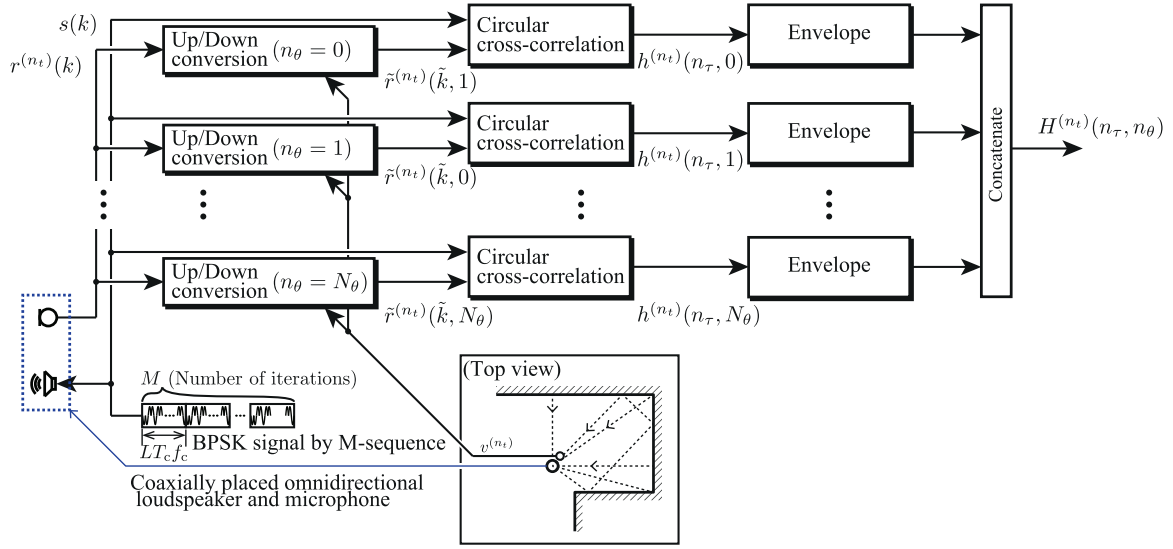
Fig. 2. Schematic diagram of the signal processing.

The Doppler effect cannot achieve the same level of angular resolution as the beam-forming method. In addition, it is impossible to determine the DoA of the reflected wave uniquely, because the Doppler effect occurs axisymmetrically around the direction of movement. It is therefore challenging to achieve stable self-position estimation without sufficient information on the DoA, which is the novelty of this research. In addition to the previously reported evaluation of the accuracy of self-position estimation in simulations [35], this article evaluates the estimation accuracy of self-position estimation in experiments.

II. PROPOSED METHODS

A. Method for Measuring ToA and DoA of Reflected Waves

Here, we describe a method for measuring the DoA of reflected waves based on the Doppler effect and the ToA based on the impulse response. This function is common to the mapping and self-localization phases described below. Fig. 2 contains a schematic diagram of the signal processing. The transmission signal generator produces a phase-modulated signal $s(k)$ using M-sequence codes. The carrier frequency is f_c, chip rate is $1/T_c$, sampling frequency is f_s, and code length of the M-sequence code is L. The transmit signal generator repeats this signal, and transmits it to the loudspeaker. The receiving signal processor records the signal received by the microphone for each block. Let $r^{(n_t)}(k)$ denote this finite-length signal. n_t is the subscript of the #n_tth received signal block measured. Crucially, the signal length of one block is $LT_c f_s M$, and the recording period is $LT_c f_s$ seconds. This setup ensures an overlap time of $LT_c f_s(M-1)$ seconds between the currently recorded block and the block recorded in the previous step. M is the number of iterations of the M-sequence code.

When the transmitter and receiver move, a Doppler effect occurs in the received acoustic signal. This reduces the correlation strength to the transmitted signal, because the signal is stretched or compressed in the time direction. The correlation strength is therefore increased by performing up/down conversion to cancel the Doppler effect. The magnitude of the Doppler shift can thus be estimated by comparing the correlation strength after the up/down conversion. These processes are denoted by

$$h^{(n_t)}(n_\tau, n_\theta) = \sum_{k_1=0}^{M-1} \sum_{k_2=0}^{L_s-1} \tilde{r}^{(n_t)}(k_1 L_s + k_2, n_\theta) s(n_\tau + k_2)$$

$$(n_\tau = 0, 1, \ldots, L_s M - 1, \; n_\theta = 0, 1, \ldots, N_\theta) \tag{1}$$

$$\tilde{r}^{(n_t)}(\tilde{k}, n_\theta) = C[r^{(n_t)}(k), \beta^{(n_t)}(n_\theta)] \tag{2}$$

$$\beta^{(n_t)}(n_\theta) = \frac{c_a - v^{(n_t)} \cos(\pi n_\theta / N_\theta)}{c_a + v^{(n_t)} \cos(\pi n_\theta / N_\theta)} \tag{3}$$

where L_s is $LT_c f_s$, $C[r(k), \beta]$ is the up/down conversion with β as the sampling ratio, c_a is the speed of sound, and $v^{(n_t)}$ is the current speed in the direction of motion. The result of the parallel envelope estimation for each n_θ in $h^{(n_t)}(n_\tau, n_\theta)$ is denoted by $H^{(n_t)}(n_\tau, n_\theta)$. The Hilbert transform was used to estimate the envelope.

B. Mapping Method

We now present a method for generating a map of global coordinates using the H measured in Section II-A. [34] First, we calculate the intensity of reflected waves at discrete positions (m_x, m_y) in Cartesian coordinates with the robot position as the origin using H. This process is denoted by

$$\hat{H}^{(n_t)}(m_x, m_y) = H^{(n_t)}(\hat{n}_\tau(m_x, m_y), \hat{n}_\theta(m_x, m_y)) \tag{4}$$

$$\hat{n}_\tau(m_x, m_y) = \text{round}\left(\frac{2f_s}{c_a} \sqrt{(m_x \Delta x_m)^2 + (m_y \Delta y_m)^2} \right) \tag{5}$$

Fig. 3.   Schematic diagram of self-positioning methods.

$$\hat{n}_\theta(m_x, m_y) = \text{round}\left(\frac{N_\theta}{\pi}\left|\arctan\left(\frac{m_y \Delta y_\mathrm{m}}{m_x \Delta x_\mathrm{m}}\right) - \phi_\mathrm{p}^{(n_t)}\right|\right) \tag{6}$$

where Δx_m and Δy_m are the grid widths of the Cartesian coordinates, $\phi_\mathrm{p}^{(n_t)}$ is the horizontal angle of the mobile robot obtained from the tracking system, and $\text{round}()$ is the conversion function to the nearest-neighbor integer. Henceforth, the 2-D array $\hat{H}$ is called an echo image. The pixel values are added after converting the elements of the echo image $\hat{H}$ measured at each time step to global coordinates. This process is denoted by

$$G(m_{x_\mathrm{g}}, m_{y_\mathrm{g}}) = \sum_{n_t=0}^{N_t} \hat{H}^{(n_t)}(m_{x_\mathrm{g}} - m_{x_\mathrm{p}}^{(n_t)}, m_{y_\mathrm{g}} - m_{y_\mathrm{p}}^{(n_t)}) \tag{7}$$

where $m_{x_\mathrm{p}}^{(n_t)}$ is $\text{round}(x_\mathrm{p}^{(n_t)}/\Delta x_\mathrm{m})$ and $m_{y_\mathrm{p}}^{(n_t)}$ is $\text{round}(y_\mathrm{p}^{(n_t)}/\Delta y_\mathrm{m})$, and $x_\mathrm{p}^{(n_t)}$ and $y_\mathrm{p}^{(n_t)}$ are the global coordinates of the robot obtained from the tracking system. Henceforth, the 2-D array G is called a map image.

C. Self-Localization Method

We can now describe the self-location estimation method using the H measured in Section II-A and the map G created in Section II-B. Fig. 3 presents a schematic diagram of the self-position estimation method. The proposed method is a particle filter-based location estimation method. The particle filter generates candidate states based on probabilities and updates them sequentially to obtain estimates. Candidate states are updated by state transitions, likelihood calculation, posterior probability distribution calculation, and resampling. The state transitions are defined using a kinematic model of a two-wheel drive

mobile robot. This kinematic model is denoted by

$$\boldsymbol{\alpha}_i^{(n_t+1)} = \begin{bmatrix} x_i^{(n_t+1)} \\ y_i^{(n_t+1)} \\ \phi_i^{(n_t+1)} \end{bmatrix} = \begin{bmatrix} x_i^{(n_t)} + (v^{(n_t)} + w_v)\Delta t \cos\phi_i^{(n_t)} \\ y_i^{(n_t)} + (v^{(n_t)} + w_v)\Delta t \sin\phi_i^{(n_t)} \\ \phi_i^{(n_t)} + (\omega^{(n_t)} + w_\omega)\Delta t \end{bmatrix} \tag{8}$$

where $x^{(n_t)}$ and $y^{(n_t)}$ are the position coordinates of the mobile robot, ϕ is the horizontal angle, $v^{(n_t)}$ and $\omega^{(n_t)}$ are the linear velocity and horizontal angular velocity of the robot, respectively, and Δt is the step time for position estimation. w_v and w_ω are defined by $w_v \sim \mathcal{N}(0, \sigma_v^2)$ and $w_\omega \sim \mathcal{N}(0, \sigma_\omega^2)$, respectively, as noise terms that follow a normal distribution. This function generates a candidate self-position after one step.

The likelihood function is defined by the mutual information between the echo image and candidate images cropped from the map image. This process is represented by

$$I_i^{(n_t)} = \sum_{k_1=0}^{K} \sum_{k_2=0}^{K} P_{\mathrm{WH},i}^{(n_t)}(k_1, k_2)\log\left(\frac{P_{\mathrm{WH},i}^{(n_t)}(k_1, k_2)}{P_{\mathrm{W},i}^{(n_t)}(k_1)P_{\mathrm{H},i}^{(n_t)}(k_2)}\right) \tag{9}$$

$$P_{\mathrm{W},i}^{(n_t)}(k) = P(W_i^{(n_t)}(m_x, m_y) = k) \tag{10}$$

$$P_{\mathrm{H},i}^{(n_t)}(k) = P(\tilde{H}_i^{(n_t)}(m_x, m_y) = k) \tag{11}$$

$$P_{\mathrm{WH},i}^{(n_t)}(k_1, k_2)$$
$$= P(W_i^{(n_t)}(m_x, m_y) = k_1, \tilde{H}_i^{(n_t)}(m_x, m_y) = k_2) \tag{12}$$

where P is the probability of satisfying the condition in parentheses, and K is the number of bins for calculating probabilities. $W_i^{(n_t)}$ is a square, cut from the map image G centered on the

position of the mobile robot, represented by

$$W_i^{(n_t)}(m_x, m_y) = \left\lfloor \frac{K}{\max\left(G_{\alpha,i}^{(n_t)}\right)} G_{\alpha,i}^{(n_t)} \right\rfloor$$

$$G_{\alpha,i}^{(n_t)} = G(m_{x\alpha,i}^{(n_t)} + m_x, m_{y\alpha,i}^{(n_t)} + m_y)$$

$$(m_x = -N_W, -N_W + 1, \ldots, N_W - 1, N_W,$$

$$m_y = -N_W, -N_W + 1, \ldots, N_W - 1, N_W) \qquad (13)$$

where $m_{x\alpha,i}^{(n_t)}$ is round$(x_i^{(n_t)}/\Delta x_m)$ and $m_{y\alpha,i}^{(n_t)}$ is round$(y_i^{(n_t)}/\Delta y_m)$. $\tilde{H}_i^{(n_t)}$ is the echo image, represented by

$$\tilde{H}_i^{(n_t)}(m_x, m_y) = \left\lfloor \frac{K}{\max\left(H_{c,i}^{(n_t)}\right)} H_{c,i}^{(n_t)} \right\rfloor$$

$$H_{c,i}^{(n_t)} = H^{(n_t)}(\tilde{n}_\tau(m_x, m_y), \tilde{n}_{\theta,i}(m_x, m_y))$$

$$(m_x = -N_W, -N_W + 1, \ldots, N_W - 1, N_W,$$

$$m_y = -N_W, -N_W + 1, \ldots, N_W - 1, N_W) \qquad (14)$$

$$\tilde{n}_\tau(m_x, m_y) = \text{round}\left(\frac{2f_s}{c_a}\sqrt{(m_x\Delta x_m)^2 + (m_y\Delta y_m)^2}\right) \qquad (15)$$

$$\tilde{n}_{\theta,i}(m_x, m_y) = \text{round}\left(\frac{N_\theta}{\pi}\left|\arctan\left(\frac{m_y\Delta y_m}{m_x\Delta x_m}\right) - \phi_i^{(n_t)}\right|\right). \qquad (16)$$

$W_i^{(n_t)}$ and $\tilde{H}_i^{(n_t)}$ generate the same number of copies as the number of candidate states.

The posterior probability distribution of self-location can be calculated from the mutual information content $I_i^{(n_t)}$ and the prior probability distribution of self-location $p(\boldsymbol{\alpha}_i^{(n-1)})$, which is represented by

$$p(\boldsymbol{\alpha}_i^{(n_t)}|H^{(n_t)}) = \frac{p(\boldsymbol{\alpha}_i^{(n_t-1)})I_i^{(n_t)}}{\sum_i^{N_s} p(\boldsymbol{\alpha}_i^{(n_t-1)})I_i^{(n_t)}} \qquad (17)$$

where N_s is the number of candidate states, and p is the probability density function. The estimated self-position is represented by

$$\hat{\boldsymbol{\alpha}}^{(n_t)} = \sum_i^{N_s} p(\boldsymbol{\alpha}_i^{(n_t)}|H^{(n_t)})\boldsymbol{\alpha}_i^{(n_t)}. \qquad (18)$$

The equation is the expected location state. The resampling process randomly extracts candidates for the next state according to the posterior probability distribution. These processes are computed sequentially to update the candidate states.

III. SIMULATION

A. Simulation Setup

We now turn to the verification of the proposed method by simulation. The simulation used a 2-D finite difference time domain (FDTD) method. The wave propagation of acoustic signals emitted from the transmitting point was calculated, and

TABLE I
SIGNAL PROCESSING PARAMETERS

Sampling frequency	f_s	40 kHz
Sequence length	L	1023
Carrier frequency	f_c	10 kHz
Chip rate	$1/T_c$	10 kHz
Number of iterations of the M-sequence code	M	6
Number of arrival directions	N	29
Grid widths of mapping	$\Delta x_m, \Delta y_m$	100 mm
Number of particles	N_s	100
Standard deviation of w_v	σ_v	0.0004 m/s
Standard deviation of w_ω	σ_ω	0.09 rad/s
Step time	Δt	0.1023 s
Number of bins	K	127

TABLE II
FDTD METHOD PARAMETERS

Grid widths of FDTD method	$\Delta x, \Delta y$	5 mm
Time step	Δt_{sim}	8.333 μs
Number of spatial cells	I, J	1000 cells
Sound speed of air	c_a	340 m/s
Density of air	ρ_0	1.293 kg/m³
Acoustic impedance of wall surface	Z_a	∞ Pa·s/m

the acoustic signals arriving at the receiving point were recorded. The moving transmitting and receiving points were implemented using the direct method [36], [37], [38]. The acoustic signals recorded at the receiving point were used for mapping and self-position estimation. Table I lists the parameters of the signal processing. The sampling frequency f_s was 40 kHz, the code length L of the M-sequence code was 1023, the carrier frequency f_c was 10 kHz, and the chip rate $1/T_c$ was 10 kHz. The number of angular divisions N_θ was 29. The grid widths of the map and echo images, Δx_m and Δy_m, respectively, were 100 mm. The number of particles N_s was 100, the variance of the speed error in the direction of movement σ_v was 0.0004 m/s, and the horizontal angular velocity error σ_ω was 0.09 rad/s.

Table II shows the parameters of the FDTD method: the grid widths, Δx and Δy, were 5 mm. The time step width Δt_{sim} was 8.333 μs. The number of cells in space was 1000×1000, the speed of sound in the air was 340 m/s, and the density of air ρ_0 was 1.293 kg/m³. The boundary condition at the edge of the simulation was a perfectly matched layer [39].

Fig. 4(a) shows the wall locations created within the simulation. The acoustic impedance of the wall surface was infinite. Fig. 4(b) shows the movement trajectory during map generation. Artifacts are reduced when the movement vector during map generation is oriented in various directions relative to the angle of the wall surfaces [34]. Therefore, a circular trajectory-based movement trajectory is used. Fig. 4(c) presents the generated map image. Fig. 5(a) indicates the linear velocity assumed to be measured by the wheel encoder on the mobile robot, and Fig. 5(b) indicates the horizontal angular velocity assumed to be measured by the same. Assuming that slippage on the floor occurred on one wheel, the horizontal angular velocity measured from the wheel encoder was set to the actual horizontal angular velocity plus a steady-state error of 0.01 rad/s. Ten trials were performed using different random seed values to check variation of the estimation error due to random numbers in the particle filter.
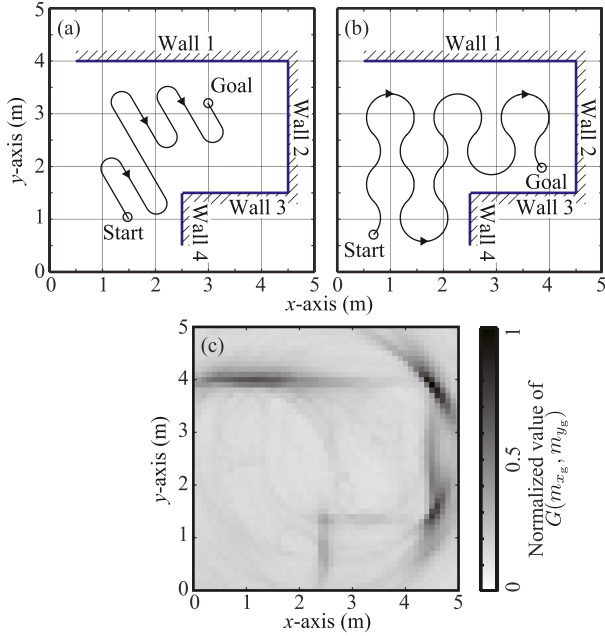
Fig. 4.   (a) Wall locations created within the simulation and movement trajectory during localization. (b) Movement trajectory during map generation. (c) Map image generated by the mapping phase.
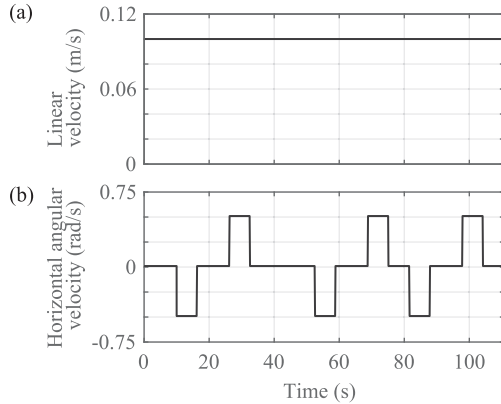

Fig. 5.   Moving speed of the robot assumed to be measured by a wheel encoder. (a) Linear velocity. (b) Horizontal angular velocity.

B. Simulation Results and Discussion

Fig. 6(a) presents the results of the self-position estimation implemented within the simulation. The blue dashed line indicates the results of position estimation using wheel odometry. Wheel odometry estimated self-position by integrating the moving speed of the mobile robot, calculated using the number of wheel revolutions. In this simulation, a steady-state error of 0.01 rad/s was intentionally generated in the horizontal angular velocity of the mobile robot, resulting in a large position estimation error due to the integral calculation. On the other hand, the proposed method using the Doppler effect for DoA estimation compensated for the error in horizontal angular velocity using reflected wave measurements, and obtained an estimation result close to the actual value. Fig. 6(b) shows the cumulative
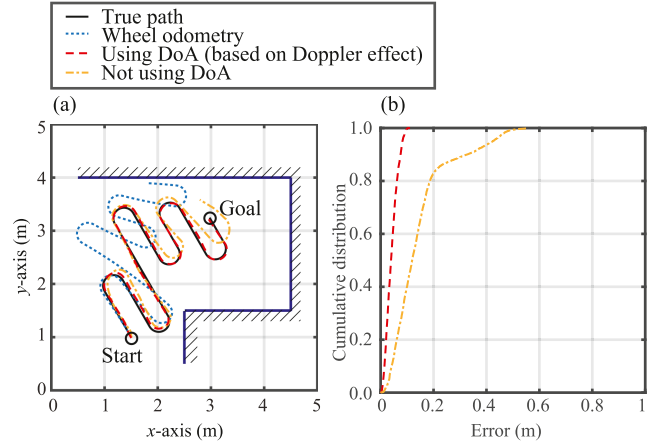
Fig. 6.   (a) Estimated positions of simulation results: Using wheel odometry (blue dotted line), DoA based on the Doppler effect and ToA based on impulse response (red dashed line), and ToA only (orange dot-dash line). (b) Cumulative density of position estimation errors. The image cropping range $N_{\mathrm{W}}\Delta x_{\mathrm{m}}$ was 4 m. ($\Delta x_{\mathrm{m}} = \Delta y_{\mathrm{m}}$).
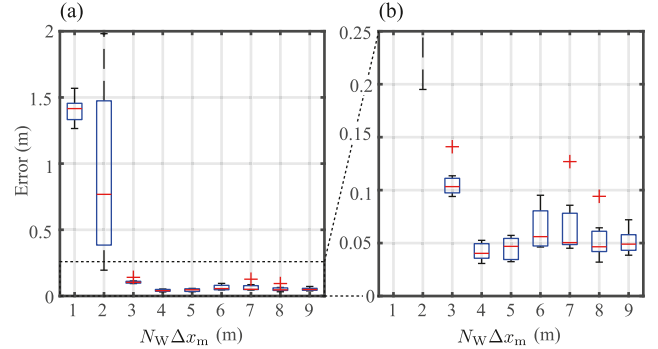
Fig. 7.   (a) Simulation results showing the relationship between image cropping range, $N_{\mathrm{W}}\Delta x_{\mathrm{m}}$, and MAE of position. (b) Enlarged view ($\Delta x_{\mathrm{m}} = \Delta y_{\mathrm{m}}$).

density of the error of the proposed method and the error of the position-estimation method using only ToA based on the impulse response. The ToA-only method used echo images in which the reflected wave intensity was concentrically distributed to estimate the position. This method cannot obtain the DoA of sound waves. The proposed method has a larger percentage of smaller errors than the method using ToA only. Therefore, use of the Doppler effect for self-position estimation is effective. An average position estimation error of 0.042 m was achieved.

Fig. 7(a) and (b) shows the relationship between the size $N_{\mathrm{W}}\Delta x_{\mathrm{m}}$ of $W_i^{(n_t)}$ and $\tilde{H}_i^{(n_t)}$ used to calculate the likelihood during position estimation and the mean absolute errors (MAEs) of position. Here, the length of $N_{\mathrm{W}}\Delta x_{\mathrm{m}}$ is related to the arrival distance of the reflected wave used to calculate the likelihood. Fig. 7(b) shows that the MAEs of position become small when $N_{\mathrm{W}}\Delta x_{\mathrm{m}}$ ranges from 4 to 5 m. This graph suggests that an optimal size exists for the image size used in the likelihood calculation.

In the proposed method, the DoA of the reflected wave is estimated from the magnitude of the Doppler shift using (3).
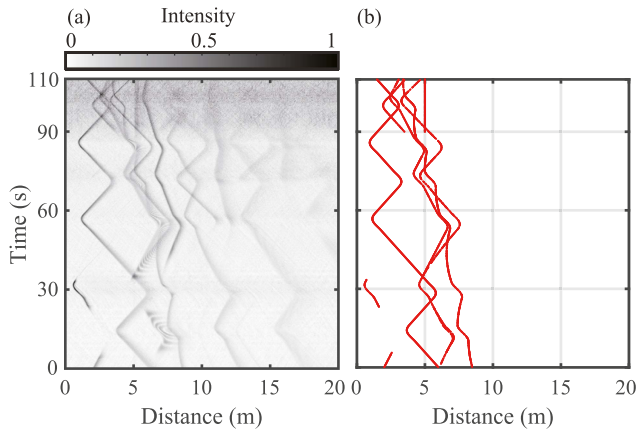
Fig. 8. (a) Normalized reflected wave intensity in simulation results; the horizontal axis is the distance converted from the ToA of the reflected wave. (b) Distance of single and double reflection paths calculated using sound ray theory.

Fig. 9. Simulation results showing the relationship between SNR and MAEs of position.

However, (3) is valid only when the angle between the direction of the sound wave emitted from the transmitter and that of the sound wave arriving at the receiver is π rad. Since the single reflection from a wall and corner reflection are sufficient conditions for (3) to be applicable, the Doppler shift can be converted to the DoA using (3) with certainty. On the other hand, other reflected waves do not satisfy the conditions for applying (3) in most cases, and such reflected waves negatively affect the accuracy of position estimation.

Fig. 8(a) shows the reflected wave intensity time course measured in the simulation. The value of this graph is $\sum_{n_\theta}^{N_\theta} H^{(n_t)}(n_\tau, n_\theta)$. The horizontal axis is the ToA of the reflected wave converted to distance, assuming a speed of sound of 340 m/s. The vertical axis shows the time elapsed since the mobile robot began moving. Fig. 8(b) reveals the distance of the reflection path calculated using sound ray theory from the location of the wall, as shown in Fig. 4(a). The maximum number of sound wave reflections is two. Corner reflections are calculated as a double reflection. Thus, the red lines in Fig. 8(b) indicate reflected waves to which (3) can be applied, and their maximum round-trip distance is about 8 m. Since the one-way distance is 4 m, many reflected waves can be effectively utilized by cropping the image size to include that range. If the image size is too large, the position estimation error also becomes large because it includes many reflected waves to which (3) cannot be applied. Therefore, it is possible to explain the value of $N_W \Delta x_m$ at which the position estimation error becomes small using the maximum round-trip distance of single and corner reflection.

Fig. 9 shows the relationship between the signal-to-noise ratio (SNR) and the MAE of the position. For this verification, it is assumed that the received signal can be represented by

$$r(k) = r_D(k) + r_R(k) + \epsilon_{add}(k) \quad (19)$$

where $r(k)$ is the continuously acquired received signal before dividing it into finite sample blocks, $r_D(k)$ is the signal propagated directly from the loudspeaker to the microphone (the signal component unaffected by the wall structure), $r_R(k)$ is the
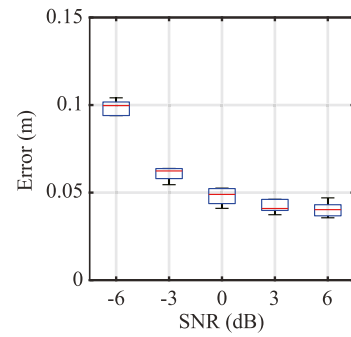
signal propagated by the reflection path, and $\epsilon_{add}(k)$ is the white noise signal intentionally added to the microphone signal. Here, the signal $r_R(k)$ reflected by the wall structure is considered the desired signal. Therefore, the power of the desired signal is defined by

$$P_s = \frac{1}{N_r} \sum_{k=1}^{N_r} (r(k) - \bar{r}_D(k) - \epsilon_{add}(k))^2 \quad (20)$$

where N_r is the number of samples of $r(k)$ from the start to the end of the measurement, and $\bar{r}_D$ is the estimated signal of the direct wave simulated in a nonreflective environment. The power of the noise signal is defined by

$$P_n = \frac{1}{N_r} \sum_{k=1}^{N_r} \epsilon_{add}(k)^2. \quad (21)$$

The magnitude of P_n controls SNR. The analysis was performed with six trials, changing the seed value to generate $\epsilon_{add}(k)$. The proposed method has a larger position estimation error when the SNR decreases. The proposed method can achieve a position estimation error of less than 0.05 m when the SNR exceeds 3 dB.

IV. EXPERIMENT

A. Experimental Setup

We here describe the experimental apparatus and environment. Fig. 10(a) shows the mobile robot created for the experiment. Two drive wheels operate the robot, each equipped with a magnetic rotary encoder. The mobile robot uses these encoders to measure the number of wheel rotations and to calculate the linear and horizontal angular velocity. The transmit signal generated by the computer is converted to an analog signal by an A–D/D–A converter (USB-6212, National Instruments), amplified by a power amplifier (AP05, FOSTEX), and emitted from the loudspeaker (PT20 K, FOSTEX). The loudspeaker had a baffle and reflector with a 0.1 m radius. A microphone (WM61 A, Panasonic) was placed on the reflector. Fig. 10(b) shows the appearance of the experimental site. A tracking system (Optitrack Prime 13X, Optitrack) was used to measure the position of the mobile robot, which was used as ground truth. An infrared reflective marker was positioned on top of the robot to measure its position using the tracking system. The
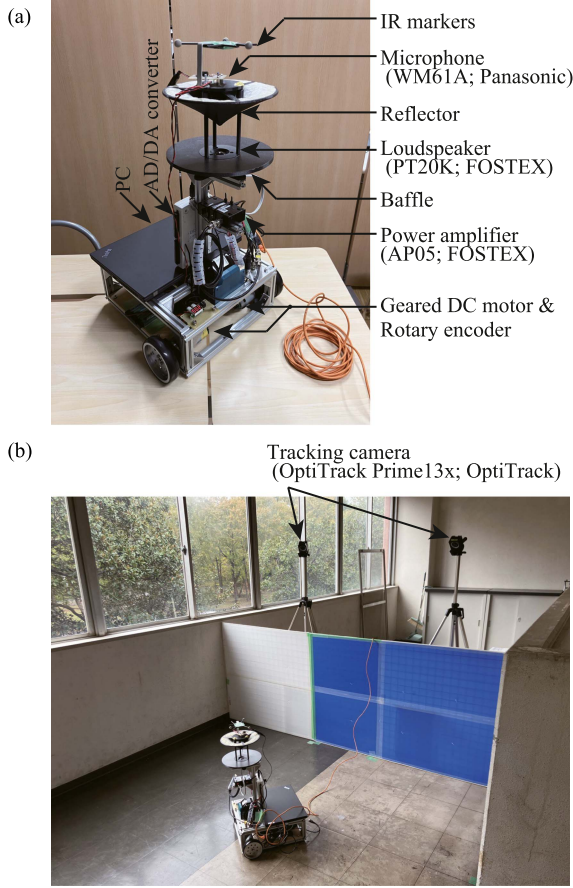
Fig. 10. (a) Overall view of the mobile robot. (b) Appearance of the experimental site.
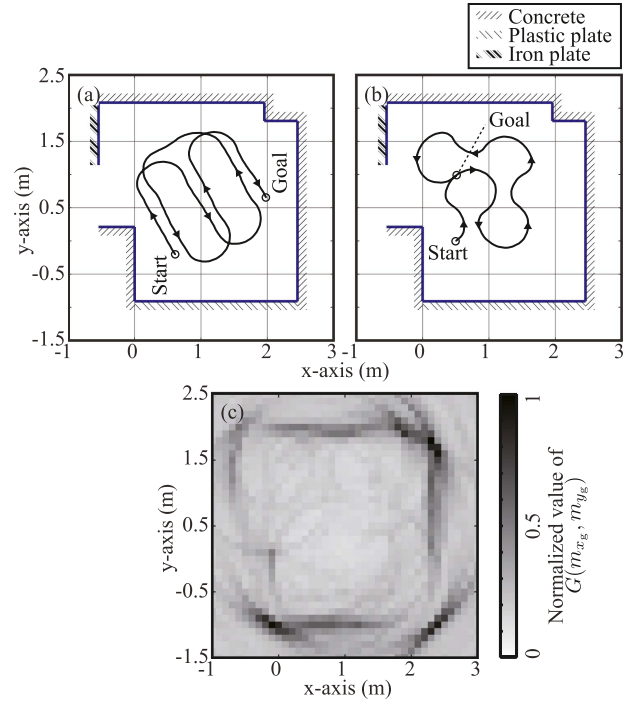

Fig. 11. (a) Location of the wall at the experimental site. (b) Movement trajectory during map generation. (c) Map image generated by the mapping phase.
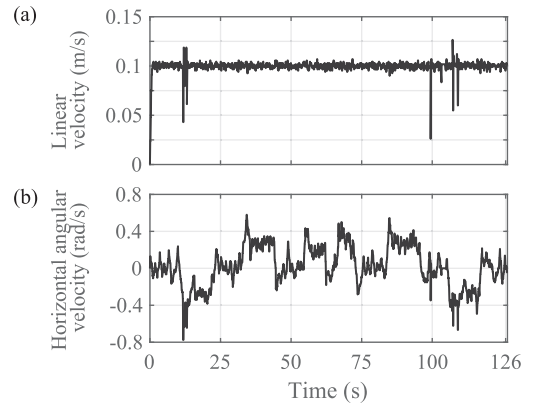

Fig. 12. Moving speed of the robot calculated from the wheel speeds when the vehicle was driven. (a) Linear velocity. (b) Horizontal angular velocity.

signal processing parameters were the same as in the simulation except for the sampling frequency, which was 50 kHz in the experiment. Fig. 11(a) shows the location of the wall at the experimental site. Fig. 11(b) shows the movement trajectory during map generation, and Fig. 11(c) shows the generated map image. Fig. 12 shows the linear velocity and horizontal angular velocity calculated from the wheel speeds when the vehicle was driven. Ten trials were performed using different random seed values to check the variation of the estimation error due to random numbers in the particle filter.

B. Experiment Results and Discussion

Fig. 13(a) presents the experimental results of self-position estimation. The wheel odometry position estimation resulted in a significant deviation from the actual value. The moving velocity measured using the wheel encoder is subject to error due to slippage between the wheel and the floor surface. Since integral calculations accumulate this error, self-position estimation using wheel odometry alone is generally difficult. On the other hand, the proposed method obtained estimation results that were as close to the actual value as the simulation results. Fig. 13(b) shows the cumulative density of position estimation errors. Similar to the simulation results, the proposed method had a larger percentage of smaller errors than the method using

ToA alone. Therefore, the experiments also showed that using the Doppler effect is effective for self-position estimation. An average position estimation error of 0.051 m was achieved.

Fig. 14(a) and (b) indicates the relationship between the size $N_{\mathrm{W}}\Delta x_{\mathrm{m}}$ of $W_i^{(n_t)}$ and $\tilde{H}_i^{(n_t)}$ used to calculate the likelihood during position estimation and the MAEs of position. As may be seen in Fig. 14(b), the MAEs of position become small when $N_{\mathrm{W}}\Delta x_{\mathrm{m}}$ ranges from 3 to 5 m. This graph suggests that an optimal size exists for the image size used in the likelihood calculation.

Fig. 15(a) shows the time course of the reflected wave intensity measured in the experiment. The horizontal axis of this graph
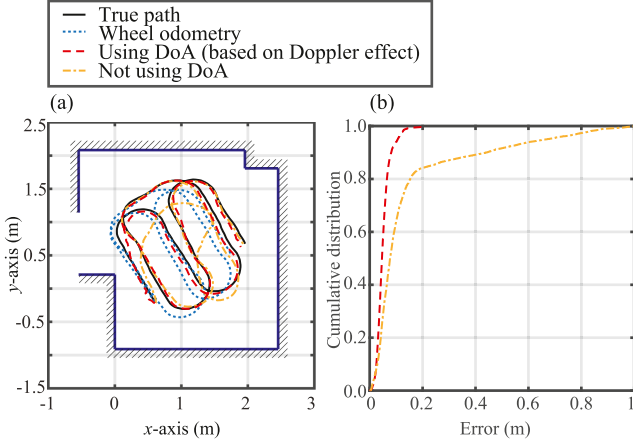
Fig. 13. (a) Estimated positions of experimental results: Using wheel odometry (blue dotted line), DoA based on the Doppler effect and ToA based on impulse response (red dashed line), and ToA only (orange dot-dash line). (b) Cumulative density of position estimation errors. The image cropping range $N_W \Delta x_m$ was 4 m ($\Delta x_m = \Delta y_m$).
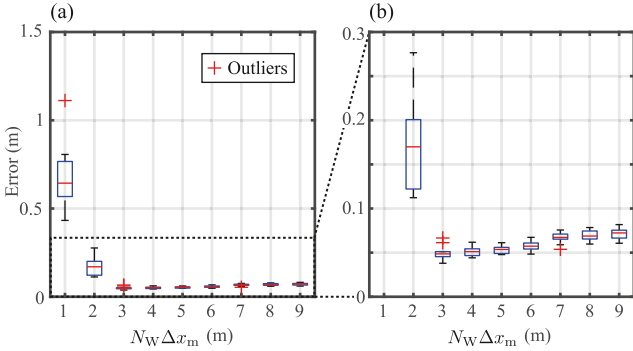

Fig. 14. (a) Experiment results showing the relationship between image cropping range $N_W \Delta x_m$ and MAE of position. (b) Enlarged view ($\Delta x_m = \Delta y_m$).
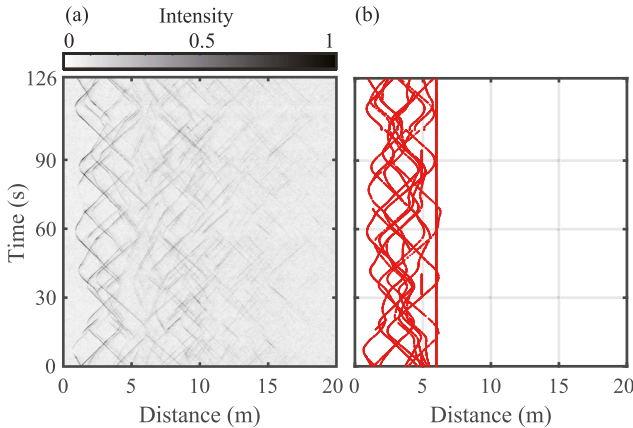
Fig. 15. (a) Normalized reflected wave intensity in experiment results; the horizontal axis is the distance converted from the ToA of the reflected wave. (b) Distance of single and double reflection paths calculated using sound ray theory.
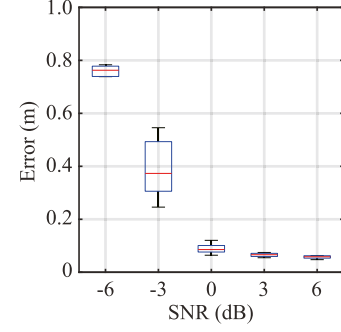

Fig. 16. Experimental results showing the relationship between SNR and MAEs of position.

is the arrival time of the reflected wave converted into the distance, assuming the speed of sound to be 340 m/s. The vertical axis indicates the time elapsed since the mobile robot started moving. Fig. 15(b) shows the distance of the reflection path calculated using sound ray theory from the location of the wall, as shown in Fig. 11(a). The red line in Fig. 15(b) indicates a reflected wave to which (3) can be applied, and its maximum round-trip distance is about 6 m. Since the one-way distance is 3 m, it is possible to effectively utilize many reflected waves by cropping the image size to include that range. Therefore, in the experiment, as in the simulation, the value of $N_W \Delta x_m$ at which the position estimation error becomes small can be explained by the maximum round-trip distance for a single reflection and corner reflection.

Fig. 16 shows the relationship between the SNR and the MAE of the position. For this verification, it is assumed that the received signal can be represented by

$$r(k) = r_D(k) + r_R(k) + \epsilon(k) + \epsilon_{add}(k) \quad (22)$$

where $\epsilon(k)$ represents the signal that includes noise generated by the microphone circuit and environmental and motion noise generated during the measurement. The equation assumed in this experiment is the same as the equation used in the simulation (19) with the addition of $\epsilon(k)$. The power of the desired signal is defined by

$$P_s = \frac{1}{N_r} \sum_{k=1}^{N_r} (r(k) - \bar{r}_D(k) - \epsilon_{add}(k))^2 \quad (23)$$

where $\bar{r}_D(k)$ is the estimated direct wave signal measured in an anechoic chamber. Recordings in the anechoic chamber were made with the transmitter and receiver mounted on the robot. It is important to note that in real-world experiments, P_s includes noise from the microphone circuitry and environmental and motion sounds generated during the measurement. The power of the noise signal is defined by

$$P_n = \frac{1}{N_r} \sum_{k=1}^{N_r} \epsilon_{add}(k)^2 \quad (24)$$

and its magnitude controls SNR. Six trials of this experiment were conducted under the same conditions. The proposed
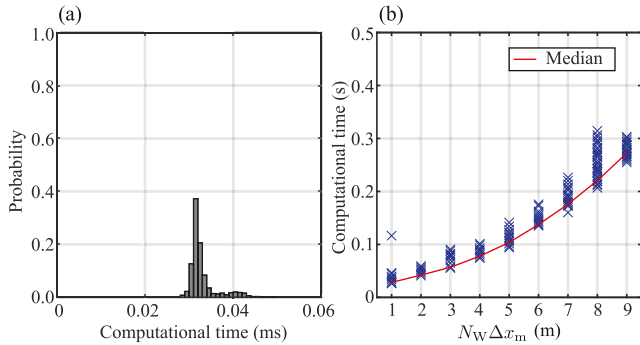
Fig. 17. (a) Computational time of the algorithm shown in Fig. 2. (b) Relationship between the computational time for one loop of the algorithm shown in Fig. 3 and the image cropping range $N_W \Delta x_m$.

method has a larger position estimation error when the SNR decreases. The proposed method can achieve a position estimation error of less than 0.1 m when the SNR exceeds 3 dB. These results suggest that controlling the transmission power according to the noise level of the environment can suppress large estimation errors even in noisy environments. In the experiment, the actual noise intensity is larger than the set noise intensity because P_s includes the power of $\epsilon(k)$. As a result, the experiment degraded the accuracy of position estimation compared with the simulation.

Fig. 17 shows the computation time of the proposed method. The computational environment was a consumer laptop computer (CPU: AMD Ryzen 7 PRO-5850 U; memory: 16 GB; Operating System: Microsoft Windows 11). The algorithm execution environment was MATLAB R2023a. Fig. 17(a) shows the computational time of the algorithm, as shown in Fig. 2. This algorithm calculates ToA and DoA from the received signal. The median computational time of this algorithm is 0.032 s. Fig. 17(b) shows the relationship between the computational time for one loop of the algorithm, as shown in Fig. 3, and the image size used for the likelihood calculation. As the image size for the likelihood calculation is increased, the computation time increases accordingly. From Fig. 14, the $N_W \Delta x_m$ at which the position estimation error is minimized is 3 m, and the median computation time in this case is 0.057 s. The algorithms in Figs. 2 and 3 can be executed sequentially on the same computer or computed independently using different computers. Either method can be used with a computation time less than the proposed method's position estimation step time ($\Delta t = 0.1023$ s). These results show the feasibility of the proposed method for real-time operation.

V. CONCLUSION

This study aimed to realize self-position estimation using only a single omnidirectional acoustic channel. The horizontal angle of the mobile robot could not be corrected using conventional measurement methods because the DoA of sound waves could not be obtained. Therefore, this article proposed a self-position estimation method that uses the DoA of reflected waves measured based on the Doppler effect and the arrival time based

on impulse response measurements. This method estimates the self-position using a map image generated in the mapping phase as a reference. Echo images are obtained based on the magnitude of the Doppler effect generated during the mobile robot's movement as the DoA and the impulse response time as the wall distance. The self-position estimation is implemented by matching the echo and map images based on the particle filter algorithm.

The accuracy of the proposed method was evaluated by simulation and experiment using the FDTD method. Both simulations and experiments showed that the proposed method could correct the position even if there were a steady-state error in the horizontal angular velocity. An average position estimation error of 0.042 m was achieved in the simulation; in the experiment, it was 0.051 m. Both simulation and experiment also confirmed that there is an optimal size setting for the matched image in the particle filter likelihood calculation. The results of this study show that using Doppler effect-based DoA measurements for self-position estimation is effective and can function as a highly accurate self-position estimator in a real environment.

REFERENCES

[1] S. Ogiso, K. Mizutani, N. Wakatsuki, and T. Ebihara, "Robust indoor localization in a reverberant environment using microphone pairs and asynchronous acoustic beacons," *IEEE Access*, vol. 7, pp. 123116–123127, 2019.

[2] S. Ogiso, K. Mizutani, N. Wakatsuki, and T. Ebihara, "Robust localization of mobile robot in reverberant rooms using acoustic beacons with iterative Bayesian filtering," in *Proc. Int. Conf. Indoor Positioning Indoor Navigation*, 2018, pp. 1–6.

[3] C. Evers and P. A. Naylor, "Acoustic SLAM," *IEEE/ACM Trans. Audio Speech, Lang. Process.*, vol. 26, no. 9, pp. 1484–1498, Sep. 2018.

[4] M. Murata, D. Ahmetovic, D. Sato, H. Takagi, K. M. Kitani, and C. Asakawa, "Smartphone-based indoor localization for blind navigation across building complexes," in *Proc. IEEE Int. Conf. Pervasive Comput. Commun.*, 2018, pp. 1–10.

[5] F. Ijaz, H. K. Yang, A. W. Ahmad, and C. Lee, "Indoor positioning: A review of indoor ultrasonic positioning systems," in *Proc. 15th Int. Conf. Adv. Commun. Technol.*, 2013, pp. 1146–1150.

[6] P. Besl and N. D. McKay, "A method for registration of 3-D shapes," *IEEE Trans. Pattern Anal. Mach. Intell.*, vol. 14, no. 2, pp. 239–256, Feb. 1992.

[7] P. Biber and W. Strasser, "The normal distributions transform: A new approach to laser scan matching," in *Proc. IEEE/RSJ Int. Conf. Intell. Robots Syst.*, 2003, pp. 2743–2748.

[8] J.-S. Gutmann and D. Fox, "An experimental comparison of localization methods continued," in *Proc. IEEE/RSJ Int. Conf. Intell. Robots Syst.*, 2002, pp. 454–459.

[9] M. U. Khan, S. A. A. Zaidi, A. Ishtiaq, S. U. R. Bukhari, S. Samer, and A. Farman, "A comparative survey of LiDAR-SLAM and LiDAR based sensor technologies," in *Proc. Mohammad Ali Jinnah Univ. Int. Conf. Comput.*, 2021, pp. 1–8.

[10] M. Zaffar, S. Ehsan, R. Stolkin, and K. M. Maier, "Sensors, slam and long-term autonomy: A review," in *Proc. NASA/ESA Conf. Adaptive Hardware Syst.*, 2018, pp. 285–290.

[11] J.-J. Lin, Y.-P. Li, W.-C. Hsu, and T.-S. Lee, "Design of an FMCW radar baseband signal processing system for automotive application," *SpringerPlus*, vol. 5, 2016, Art. no. 42.

[12] R. Kuc and M. W. Siegel, "Physically based simulation model for acoustic sensor robot navigation," *IEEE Trans. Pattern Anal. Mach. Intell.*, vol. PAMI- 9, no. 6, pp. 766–778, Nov. 1987.

[13] A. Elfes, "Sonar-based real-world mapping and navigation," *IEEE J. Robot. Autom.*, vol. 3, no. 3, pp. 249–265, Jun. 1987.

[14] D. Marioli, E. Sardini, and A. Taroni, "Ultrasonic distance measurement for linear and angular position control," *IEEE Trans. Instrum. Meas.*, vol. 37, no. 4, pp. 578–581, Dec. 1988.

[15] J. Crowley, "World modeling and position estimation for a mobile robot using ultrasonic ranging," in *Proc. Int. Conf. Robot. Autom.*, 1989, pp. 674–680.

[16] L. Kleeman and R. Kuc, "Mobile robot sonar for target localization and classification," *Int. J. Robot. Res.*, vol. 14, no. 4, pp. 295–318, 1995.

[17] J. Borenstein and Y. Koren, "The vector field histogram-fast obstacle avoidance for mobile robots," *IEEE Trans. Robot. Autom.*, vol. 7, no. 3, pp. 278–288, Jun. 1991.

[18] H. Peremans, K. Audenaert, and J. Van Campenhout, "A high-resolution sensor based on tri-aural perception," *IEEE Trans. Robot. Autom.*, vol. 9, no. 1, pp. 36–48, Feb. 1993.

[19] P. Chakravarthula, J. D'Souza, E. Tseng, J. Bartusek, and F. Heide, "Seeing with sound: Long-range acoustic beamforming for multimodal scene understanding," in *Proc. IEEE/CVF Conf. Comput. Vis. Pattern Recognit.*, 2023, pp. 982–991.

[20] A. Jiménez Martín et al., "EMFi-based ultrasonic sensory array for 3D localization of reflectors using positioning algorithms," *IEEE Sensors J.*, vol. 15, no. 5, pp. 2951–2962, May 2015.

[21] O.-L. Ouabi, P. Pomarede, M. Geist, N. F. Declercq, and C. Pradalier, "A fastSLAM approach integrating beamforming maps for ultrasound-based robotic inspection of metal structures," *IEEE Robot. Autom. Lett.*, vol. 6, no. 2, pp. 2908–2913, Apr. 2021.

[22] J. Pareja-Contreras, M. Sotomayor-Polar, and E. Zenteno-Bolanos, "Beamforming echo-localization system using multitone excitation signals," in *Proc. 2nd Int. Symp. Instrum. Syst., Circuits Transducers*, 2017, pp. 1–5.

[23] S. Chowdhury, M. Ahmadi, and W. Miller, "Design of a MEMS acoustical beamforming sensor microarray," *IEEE Sensors J.*, vol. 2, no. 6, pp. 617–627, Dec. 2002.

[24] Y. Qiu, Y. Jiang, B. Wang, and Z. Huang, "An analytical method for 3-D target localization based on a four-element ultrasonic sensor array with TOA measurement," *IEEE Sens. Lett.*, vol. 7, no. 5, May 2023, Art. no. 6002104.

[25] S. Koyama, K. Okubo, and N. Tagawa, "Acoustic sensing method for an occlusion area with super-directional sound sources and multiple modulation signal," *Japanese J. Appl. Phys.*, vol. 60, no. SD, Jun. 2021, Art. no. SDDB09.

[26] Y. Asakura, K. Okubo, and N. Tagawa, "Experimental evaluation of long-range acoustic sensing using super-directivity speaker and super-resolution signal processing with pulse compression technique," *Japanese J. Appl. Phys.*, vol. 56, no. 7S1, Jun. 2017, Art. no. 07JC14.

[27] M. Kreković, I. Dokmanić, and M. Vetterli, "EchoSLAM: Simultaneous localization and mapping with acoustic echoes," in *Proc. IEEE Int. Conf. Acoust., Speech Signal Process.*, 2016, pp. 11–15.

[28] M. Kreković, I. Dokmanić, and M. Vetterli, "Omnidirectional bats, point-to-plane distances, and the price of uniqueness," in *Proc. IEEE Int. Conf. Acoust., Speech Signal Process.*, 2017, pp. 3261–3265.

[29] W. Luo, Q. Song, Z. Yan, R. Tan, and G. Lin, "Indoor smartphone SLAM with acoustic echoes," *IEEE Trans. Mobile Comput.*, vol. 23, no. 6, pp. 6634–6649, Jun. 2024.

[30] A. Tsuchiya, N. Wakatsuki, T. Ebihara, K. Zempo, and K. Mizutani, "Indoor self-localization using multipath arrival time measured by a single acoustic ranging sensor," *Japanese J. Appl. Phys.*, vol. 61, no. SG, May 2022, Art. no. SG1037.

[31] A. Tsuchiya, N. Wakatsuki, T. Ebihara, K. Zempo, and K. Mizutani, "Indoor self-localization of mobile robots using asynchronous acoustic multipath arrival time measurement," in *Proc. IEEE 11th Glob. Conf. Consum. Electron.*, 2022, pp. 177–181.

[32] E. G. Sarabia, J. R. Llata, S. Robla, C. Torre-Ferrero, and J. P. Oria, "Accurate estimation of airborne ultrasonic time-of-flight for overlapping echoes," *Sensors*, vol. 13, no. 11, pp. 15465–15488, 2013.

[33] A. Tsuchiya, N. Wakatsuki, T. Ebihara, K. Zempo, and K. Mizutani, "Time-of-arrival measurement method for reflected waves from multiple directions using Doppler effect by a single coaxially placed omni-directional SP and MIC," in *Proc. 29th Int. Congr. Sound Vib.*, 2023, pp. 1–8.

[34] A. Tsuchiya, N. Wakatsuki, T. Ebihara, K. Zempo, and K. Mizutani, "Method of reconstructing wall positions using direction-of-arrival estimation based on the Doppler effect of omnidirectional active sonar," in *Proc. Work-in- Prog. Papers at 13th Int. Conf. Indoor Positioning Indoor Navigation*, 2023, pp. 1–12.

[35] A. Tsuchiya, N. Wakatsuki, T. Ebihara, K. Zempo, and K. Mizutani, "Self-localization method using time-of-arrival and direction-of-arrival of sound waves measured based on the Doppler effect," in *The 44th Symp. Ultrason. Electron.*, 2023, pp. 9–10.

[36] T. Tsuchiya and M. Kanamori, "Moving sound source with an arbitrary trajectory in the two-dimensional finite-difference time-domain method," *Japanese J. Appl. Phys.*, vol. 60, no. SD, Mar. 2021, Art. no. SDDB02.

[37] T. Tsuchiya, Y. Teshima, and S. Hiryu, "Two-dimensional finite difference-time domain simulation of moving sound source and receiver," *Acoustical Sci. Technol.*, vol. 43, no. 1, pp. 57–65, 2022.

[38] O. Yamashita, T. Tsuchiya, Y. Iwaya, M. Otani, and Y. Inoguchi, "Reflective boundary condition with arbitrary boundary shape for compact-explicit finite-difference time-domain method," *Japanese J. Appl. Phys.*, vol. 54, no. 7S1, Jun. 2015, Art. no. 07HC02.

[39] Q. Qi and T. L. Geers, "Evaluation of the perfectly matched layer for computational acoustics," *J. Comput. Phys.*, vol. 139, no. 1, pp. 166–183, 1998.

Atsushi Tsuchiya (Graduate Student Member, IEEE) received the master's degree in engineering in 2022 from the University of Tsukuba, Tsukuba, Japan, where he is currently working toward the Ph.D. degree.

His research interests include self-localization using acoustic echo, ultrasound electronics, mobile robotics engineering, and civil engineering.

Dr. Tsuchiya is a Research Fellow with the Japan Society for the Promotion of Science (DC1), Japan. He is a Student Member of the Japan Society of Civil Engineering. He was the recipient of the Best Poster Award in the 13th International Conference on Indoor Positioning and Indoor Navigation (IPIN2023).

Naoto Wakatsuki received the B.Eng., M.Eng., and D.Eng. degrees in engineering from the University of Tsukuba, Tsukuba, Japan, in 1993, 1995, and 2004, respectively.

He was with Okayama University, from 1995 to 2001, and with Akita Prefectural University, from 2001 to 2006. He is currently a Full Professor with the Institute of Systems and Information Engineering, University of Tsukuba. His research interests include acoustic instrumentation, simulation-based visualization, vibration sensors and actuators, acoustical engineering, musical acoustics, and inverse problems.

Dr. Wakatsuki was with the Acoustical Society of Japan, the Acoustical Society of America, the Society of Agricultural Structures, and the Japan Society for Simulation Technology.

Tadashi Ebihara (Senior Member, IEEE) received the Ph.D. degree in engineering from the University of Tsukuba, Tsukuba, Japan, in 2010.

From September 2013 to December 2013, he was a Visiting Professor with the Delft University of Technology, Delft, The Netherlands. He is currently an Associate Professor with the Institute of Systems and Information Engineering, University of Tsukuba. His research interests include mobile communications and their applications to underwater acoustic communication systems.

Dr. Ebihara was the recipient of the Research Fellowship for Young Scientists (DC1) from the Japan Society for the Promotion of Science (JSPS) for the years 2009 and 2010, and the 2017 IEEE Oceanic Engineering Society Japan Chapter Young Researcher Award.
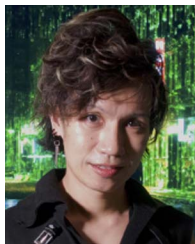
Keiichi Zempo (Member, IEEE) received the B.Sc. degree in physics from the College of Natural Science, University of Tsukuba, Tsukuba, Japan, in 2008, the M.B.A. degree in business administration from the Department of Business Administration and Public Policy, University of Tsukuba, in 2010, and the Ph.D. degree in engineering from the Department of Intelligent Interaction Technologies, University of Tsukuba, in 2013.

From 2013 to 2014, he was with the Center for Service Engineering, National Institute of Advanced Industrial Science and Technology. He is currently an Associate Professor with the University of Tsukuba, a PRESTO Researcher with Japan Science and Technology Agency, Kawaguchi, Japan, and a CEO with Xtrans Tech Inc. His research interests include human augmentation, sense substitution, service engineering, telepresence, and xR.

Dr. Zempo is a Member of the Association for Computing Machinery, the Acoustics Society of Japan, the Society for Serviceology, the Japanese Society for Artificial Intelligence, and the Virtual Reality Society of Japan.

Koichi Mizutani received the graduation degree from the National Defense Academy (NDA), Yokosuka, Japan, in 1979, and the Ph.D. degree in engineering from Kyoto University, Kyoto, Japan, in 1990.

He was a Researcher with the Department of Electrical Engineering, NDA, from 1984 to 1988, and with the Department of Research, Communication and Intelligence School, Japanese Ground Self Defense Force (JGSDF) from 1988 to 1990. From 1991 to 1992, he was the Deputy Director of the Secretariat of the Director General with the National Defense Agency. He retired from the JGSDF at the rank of Major. He joined the faculty of the Institute of Applied Physics, University of Tsukuba, as an Assistant Professor in 1992, and bacame an Associate Professor in 1998, and a Full Professor in 2004. Since 2021, he was a Researcher (full time) with the Faculty of Engineering, Information and Systems, University of Tsukuba. In 2021, he was given the title of a Professor Emeritus by the University of Tsukuba. His research interests included ultrasonic electronics, medical electronics, welfare technologies, complementation of human sensory functions, robot sensing, communication systems in sensing grids, environment monitoring, applied optics, applied acoustics, musical acoustics, food and agricultural engineering, and the health monitoring engineering of livestock.

Dr. Mizutani was a Member of the Acoustics Society of Japan, the Marine Acoustics Society of Japan, the Society of Agricultural Structures, Japan, the Japan Society of Civil Engineering, and the Japan Society of Applied Physics.